Electrochemistry
The Electrochemical Society of Japan
Received: March 9, 2026
Accepted: May 8, 2026
Published online: May 12, 2026
Issued: June 4, 2026
https://doi.org/10.5796/electrochemistry.26-00020
Article
Electrochemistry, 94(6), 067001 (2026)

Effects of Reaction Conditions on Topochemical F-doping to $La_{0.6}Sr_{0.4}CoO_{3-\delta}$ Thin Films†

Takuya KATSUMATA,[a,*,§] Chayathorn LAWTHAWEESAWAT,[b,c] Mahunnop FAKKAO,[c] Yuta KIMURA,[a,§] Takashi NAKAMURA,[d,§] and Koji AMEZAWA[a,§§]

[a] Institute of Multidisciplinary Research for Advanced Materials, Tohoku University, 2-1-1 Katahira Aoba-ku, Sendai 980-8577, Japan
[b] Department of Mechanical Engineering, Tohoku University, 6-6-01 Aoba, Aramaki, Aoba-ku, Sendai 980-8579, Japan
[c] Advanced Mobility and Propulsion Research Laboratory, Faculty of Engineering, Thai-Nichi Institute of Technology, 1771/1 Pattanakarn Rd. Suanluang, Bangkok, 10250, Thailand
[d] Institute of Materials and Systems for Sustainability, Nagoya University, Furo-cho, Chikusa, Nagoya 464-8601, Japan

* Corresponding author: takuya.katsumata.e1@tohoku.ac.jp

ABSTRACT

Anion doping is a promising approach for controlling material functionalities. However, precise control of anion concentration remains challenging. In this study, we experimentally evaluated the effects of reaction conditions on F concentration and distribution in topochemical F doping to $La_{0.6}Sr_{0.4}CoO_{3-\delta}$ thin films by simply varying F sources, reaction temperatures, and reaction times. Comparative experiments using MgF_2, BiF_3 and PVDF as F sources suggested that the equilibrium F_2 activity of the F source is the primary factor governing the F concentration in the product. Meanwhile, the choice of F source also significantly affects the homogeneity of F distribution. Temperature-dependent experiments showed that maximum F incorporation was achieved at 300 °C, while higher temperatures led to F release and decreased F concentration. Time-dependent experiments demonstrated that F concentration increases with prolonged reaction time. Notably, uniform F distribution throughout the entire film thickness (100–150 nm) was achieved within just 1-hour treatment at 240 °C when using MgF_2 as the F source, indicating that the topochemical F-doping process is governed by surface reaction kinetics rather than bulk diffusion. These findings enable precise control of anion composition in topochemical anion doping and contribute to the rational design of functional materials by anion doping.

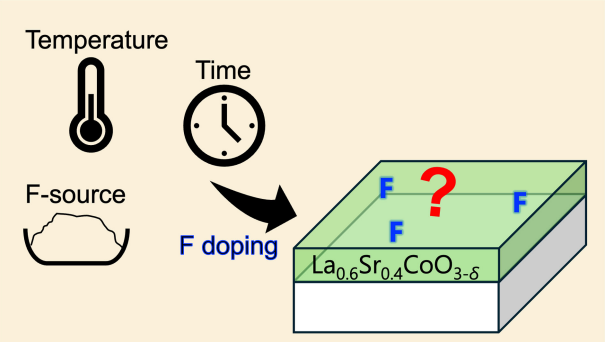

Keywords : Anion Doping, F Doping, Topochemical Method, Mixed-anion Compounds

1. Introduction

Anion doping has attracted attention as a novel strategy for controlling material functionalities. By incorporating anion species with different ionic radii and electronegativity into crystal structures, unique properties that cannot be achieved through conventional cation control are expected.[1,2] Functional improvements through anion doping have been reported in various material fields such as battery materials and catalytic materials.[3–5] For example, significant capacity enhancement has been reported by F doping into lithium-ion battery cathode materials,[6] and improved electrocatalytic activity has been demonstrated by F or S doping.[7–9]

However, precise control of anion composition remains a significant challenge, limiting the fundamental understanding of anion composition–material functionality relationships. The most common anion doping method is the solid-state reaction, which involves mixing precursors and reacting them at high temperature. However, the accessible compositional range is limited due to differences in vapor pressure and reactivity among anionic constituent elements.[1] To overcome these constraints, methods utilizing special reaction environments have been developed, including high-pressure synthesis,[10–12] solvothermal methods,[13–15] mechanical milling,[16–18] electrochemical methods[19,20] and topochemical approaches.[21]

Among these methods, the topochemical approach is widely used because it enables substitution and insertion of specific anion species while maintaining the crystal structure framework.[22,23] This method has been applied to the introduction of fluoride ions,[23,24] hydride ions,[22,25] nitride ions,[26,27] and others. In topochemical F doping, F_2 gas,[28,29] fluoropolymers (such as polyvinylidene fluoride (PVDF)[23,24,30–32] and polytetrafluoroethylene (PTFE)[33,34]) and inorganic F sources such as XeF_2[28,35] and MgF_2[36] are commonly used. However, the reported reaction conditions are extremely diverse, such as temperatures and reaction times. While it is evident that optimization of reaction conditions is necessary depending on the target composition, systematic experimental studies on how F source, reaction temperature, and reaction time affect the F-doping process have not been performed. The absence of comprehensive

†The content of this paper will be published by Takuya Katsumata as a PhD thesis at Tohoku University in 2026.
§ECSJ Active Member
§§ECSJ Fellow

T. Katsumata orcid.org/0009-0002-7532-6198
M. Fakkao orcid.org/0000-0002-3637-3701
Y. Kimura orcid.org/0000-0002-3525-1366
T. Nakamura orcid.org/0000-0001-5461-9958
K. Amezawa orcid.org/0000-0002-3430-6927

thermodynamic and kinetic understanding hinders strategic material functionality design through topochemical F doping.

In this study, we experimentally investigated the effects of simple changes in reaction conditions, namely F source, reaction temperature, and reaction time, on topochemical F doping by using $La_{0.6}Sr_{0.4}CoO_{3-\delta}$ (LSC64) thin films as a model system. LSC64 is a representative perovskite oxide with O vacancies and mixed ionic-electronic conductivity, making it suitable for studying anion doping reactions.[37,38] The use of thin film samples enables precise analysis of F distribution within the sample. The insights obtained in this study will establish practical guidelines for optimizing topochemical F doping conditions and enable strategic control of anion composition and material functionality.

2. Experiments

2.1 Fabrication of the LSC64 thin film

The LSC64 thin films were fabricated by pulsed laser deposition (PLD). LSC64, the target material of PLD, was synthesized by solid state reaction method. Stoichiometric amounts of La_2O_3 (99.99 %, Wako Pure Chemical Industries, Ltd.), $Sr(NO_3)_2$ (99.9 %, Kanto Chemical Co.), Co_3O_4 (99.99 %, Japan Pure Chemical Laboratory Co., Ltd.) were mixed in mortar, pelletized and calcined at 1200 °C for 12 h. The obtained pellet was crushed, pelletized again and sintered at 1200 °C for 12 h. The obtained LSC64 pellet was used for the PLD target. 8 mol% Y_2O_3-doped ZrO_2 (YSZ, Tosoh Co.) dense pellet was used for the substrate of the LSC64 thin film deposition. YSZ powder was pelletized using a φ25 die and sintered at 1600 °C for 6 h. The YSZ pellets were polished by diamond suspension (particle diameter: 45, 9, 6, 3, 1 µm). The films were deposited at 700 °C under an O_2 partial pressure of 1.0 Pa. The distance between the substrate and the target was maintained at 40 mm. The deposition time was maintained for 15 min at a repetition rate of 10 Hz and a laser power of 170 mW. After the deposition, the film samples were annealed at 700 °C for 1 h and cooled naturally to 25 °C without changing the chamber atmosphere.

2.2 Topochemical F doping to the LSC64 thin films

The substrate-supported thin films were subjected to F doping by the topochemical method. The LSC64 thin film and a F source were separately placed in an alumina boat within an Ar-sealed glass tube and subsequently heated (Fig. 1). To investigate the effect of F sources, the film was co-heated with 0.05 g of MgF_2 (99.9 %, Thermo Scientific), BiF_3 (99.9 %, Japan Pure Chemical Laboratory Co., Ltd.), or PVDF (Sigma-Aldrich) at 240 °C for 10 h. To investigate the effect of reaction temperature, the film was co-heated with 0.05 g of MgF_2 at 240, 300, 350, or 500 °C for 10 h. To investigate the effect of reaction time, the film was co-heated with 0.05 g of MgF_2 at 240 °C for 1, 10, or 40 h.

2.3 Characterization of the F-doped thin films

The thickness of the thin films was evaluated by a stylus profiler (Dektak XT, Bruker). The crystal structure of the thin films was characterized by x-ray diffractometry (XRD, D8 Advance, Bruker) using Cu*Kα* x-ray source. The lattice parameters were calculated by CellCalc software.[39] F1s spectra were obtained by x-ray photoelectron spectroscopy (XPS, ESCA3400, Shimadzu) using Mg*Kα* x-ray source (10 kV and 10 mA). Elemental distributions in the thin films were evaluated by time-of-flight secondary ion mass spectrometry (TOF-SIMS, TOF.SIMS5, ION-TOF) utilizing a 25 kV Bi_3^{2+} primary ion source (field of view 10 µm × 10 µm). The thin film pellet was fixed on a carbon tape and ablated with a 1 kV Cs^+ sputtering ion beam (crater size 100 µm × 100 µm). F-concentration was measured by field emission electron probe microanalyzer (FE-EPMA, JXA-8530F, JEOL) operating at an accelerating voltage of 12 kV using thin film analysis program (XM-27470THIN). Scanning electron microscopy (SEM) observation was conducted by using the same equipment and condition. X-ray absorption spectroscopy (XAS) was carried out at BL08W in NanoTerasu, Japan. XAS spectra at Co *K*-edges were recorded by the partial fluorescence yield mode.

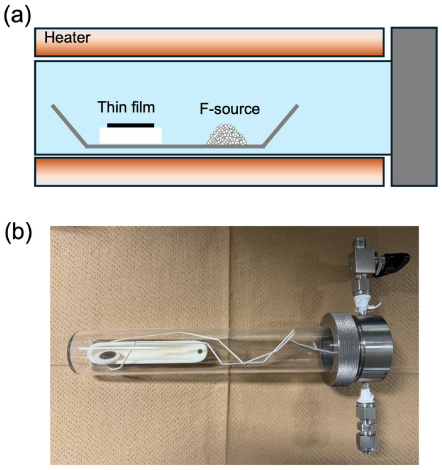

Figure 1. (a) Schematic illustration and (b) photograph of the chamber used for the topochemical F-doping to the LSC64 thin films.

3. Results and Discussion

3.1 Effects of F sources

To investigate the effect of F sources on the topochemical F-doping process, LSC64 thin films were heat-treated with MgF_2, BiF_3 or PVDF at 240 °C for 10 h. These F sources were selected based on their different equilibrium F_2 activities (a_{F_2}) because the equilibrium a_{F_2} is expected to determine the F concentration in the product material. The equilibrium a_{F_2} values at 240 °C, calculated using a thermodynamic database MALT are 7.94×10^{-106} for MgF_2 (reaction: $MgF_2 = Mg + F_2$) and 7.66×10^{-54} for BiF_3 (reaction: $2/3BiF_3 = 2/3Bi + F_2$).[40] PVDF has been reported as a strong F doping agent and is expected to achieve an even higher equilibrium a_{F_2} with strong reducing conditions.[32,41,42]

Profilometry measurements revealed that the thickness of the LSC64 pristine thin films was 100–150 nm. SEM observation confirmed the formation of dense thin films without pinholes or cracks (Fig. 2a). XRD analysis of the pristine thin films showed diffraction patterns corresponding to the perovskite LSC64 phase and the YSZ substrate, with no preferred orientation along specific crystal planes, indicating the formation of polycrystalline films (Fig. 2e).

Figures 2a–2d show the SEM images of the pristine and the F-doped LSC64 thin films treated with MgF_2, BiF_3, or PVDF at 240 °C for 10 h. No significant changes in surface morphology were observed after F doping, indicating that the topochemical F doping process does not affect the film surface. Figure 2e shows the XRD patterns of these samples. For all samples, only peaks corresponding to the YSZ substrate and the LSC64 perovskite phase were observed, with no crystalline impurity phases detected. This indicates that no side reactions occurred during the F-doping treatment. Compared to the pristine sample, all F-doped samples exhibited a shift of the LSC64 peaks toward lower angles, suggesting lattice expansion. From the obtained XRD patterns, the lattice parameters were refined assuming a cubic structure with space group $Pm\bar{3}m$. The obtained lattice parameters were 3.729, 3.760, 3.753 and 3.789 Å for the pristine, MgF_2-, BiF_3- and PVDF-treated samples, respectively (Table 1). This shows that the degree

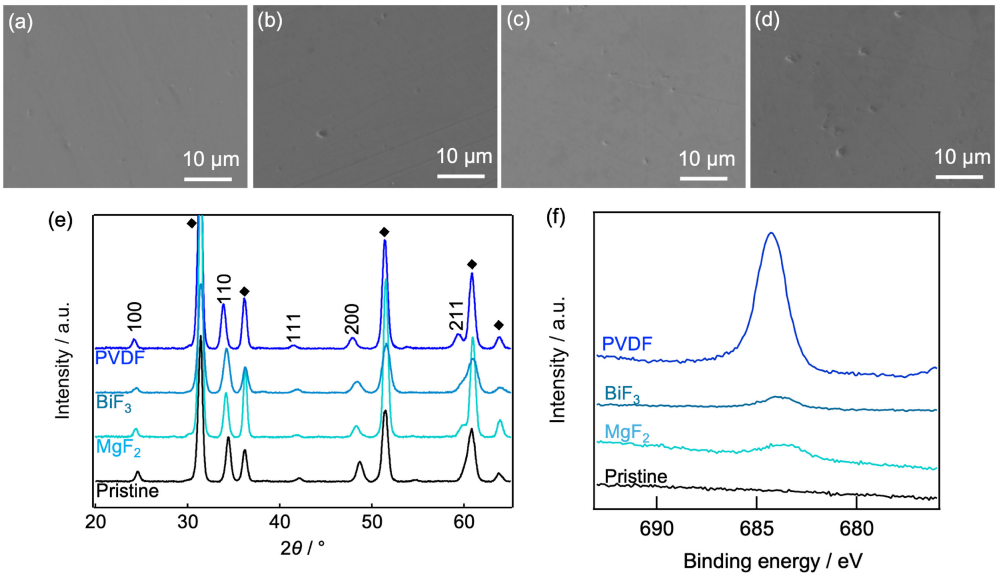

Figure 2. SEM images showing the top surface of (a) the pristine and the F-doped LSC64 thin films treated with (b) MgF_2, (c) BiF_3 or (d) PVDF at 240 °C for 10 h. (e) XRD patterns of the pristine and the F-doped LSC64 thin films. The LSC64 peaks were indexed based on the cubic perovskite structure with space group $Pm\bar{3}m$. The symbol (◆) represents YSZ (substrate) peaks. (f) XPS F1s spectra of each sample.

Table 1. Equilibrium a_{F_2} of F sources, lattice parameters, and F concentration ratios ($C_F/(C_{La}+C_{Sr})$) of the F-doped LSC64 thin films under different F source, temperature, and time conditions. Lattice parameters were calculated assuming the space group $Pm\bar{3}m$ (cubic) for LSC64. Equilibrium a_{F_2} values of fluorides were calculated using the thermodynamic database MALT.[40] F concentration ratios were calculated from atomic concentrations (at%) measured by EPMA.

F source	Temperature /°C	time/h	Equilibrium a_{F_2} of F source	Lattice parameter a/Å	Concentration ratio $C_F/(C_{La}+C_{Sr})$
None (Pristine)	240	10	—	3.729(22)	—
PVDF	240	10	No data	3.789(26)	0.33 ± 0.03
BiF_3	240	10	7.66×10^{-54}	3.753(24)	0.17 ± 0.03
MgF_2	240	10	7.94×10^{-106}	3.760(25)	0.22 ± 0.02
MgF_2	300	10	7.03×10^{-94}	3.788(24)	0.29 ± 0.03
MgF_2	350	10	1.10×10^{-85}	3.779(23)	0.26 ± 0.03
MgF_2	500	10	1.75×10^{-67}	3.749(27)	0.09 ± 0.02
MgF_2	240	1	7.94×10^{-106}	3.736(21)	0.05 ± 0.01
MgF_2	240	40	7.94×10^{-106}	3.804(22)	0.43 ± 0.04

of lattice expansion followed the order: pristine < BiF_3 < MgF_2 < PVDF. Notably, the BiF_3-treated sample showed broader peak widths compared to the other samples, suggesting an increase in micro strains.

XPS measurements were performed to confirm F incorporation. As shown in Fig. 2f, F1s peaks were detected in all the F-doped samples, confirming successful F doping at least on the surface. To evaluate the F concentration and distribution throughout the film thickness, depth-profiling compositional analysis was conducted by TOF-SIMS. In the pristine sample, the F^- intensity was below the detection limit. In contrast, F^- signals were detected throughout the entire film thickness in all the F-doped thin films, indicating successful F incorporation into the bulk (Fig. 3). However, notable differences in F^- distributions were observed among the samples. The PVDF- and MgF_2-treated samples showed the relatively uniform F distribution throughout the film thickness. In contrast, the BiF_3-treated sample showed the non-uniform F distribution, the F^- intensity decreased with the distance from the surface where F was supplied. Consequently, while the surface F concentration of the BiF_3-treated sample was higher than that of the MgF_2-treated sample, it was lower in the deeper bulk region. The bulk F concentration ratios ($C_F/(C_{La}+C_{Sr})$) measured by EPMA were 0.33, 0.22, and 0.17 for PVDF-, MgF_2-, and BiF_3-treated samples, respectively (Table 1). Here, C_X denotes the atomic concentration of element X (X = La, Sr, F) measured by EPMA. The F concentration order (BiF_3 < MgF_2 < PVDF) showed that PVDF, having the highest equilibrium a_{F_2}, yielded the highest F concentration as expected. However, the F concentration order between MgF_2 and BiF_3 was opposite to their equilibrium a_{F_2}. This is likely attributed to the gradient F distribution in the BiF_3-treated sample and hindered F diffusion into the interior due to some reaction occurring at the film surface.

To investigate the charge compensation mechanism during the F doping, Co *K*-edge XAS measurements were performed. Figure 4 shows the Co *K*-edge x-ray absorption near edge structure (XANES) spectra for each sample. The position of the Co *K*-edge white line shifted toward lower energy in the order: PVDF < MgF_2/BiF_3 < pristine, indicating progressive reduction of Co.[43] The PVDF-treated

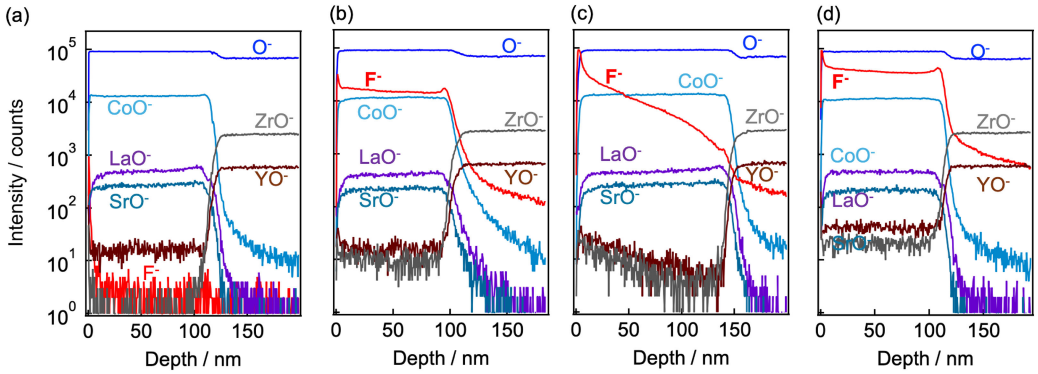

Figure 3. In-depth elemental profiles evaluated by TOF-SIMS of (a) the pristine and the F-doped LSC64 thin films treated with (b) MgF_2, (c) BiF_3 or (d) PVDF at 240 °C for 10 h.

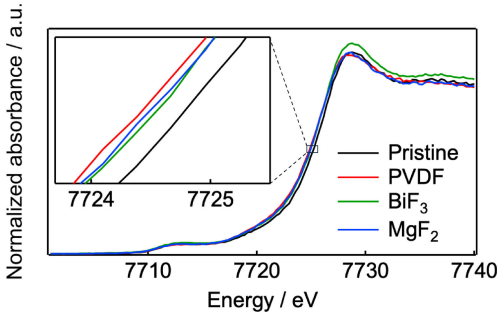

Figure 4. XANES spectra of Co *K*-edge of the pristine and the F-doped LSC64 thin films treated with MgF_2, BiF_3 or PVDF. The inset shows the expanded spectra around the absorption edge.

sample exhibited the most extensive reduction of Co. This reduction of Co is expected to cause lattice expansion, which is consistent with the XRD results showing the largest lattice parameter in the PVDF-treated sample.

The observed Co reduction provides important insights into the F doping mechanism. Theoretically, the incorporation of F into O vacancy sites should result in oxidation of the host cations as shown in Eq. 1,

$$V_O^{\cdot\cdot} + \frac{1}{2}F_2(g) + Co_{Co}^{\times} \rightarrow F_O^{\cdot} + Co_{Co}^{\cdot} \quad (1)$$

where defect species are expressed by Kröger–Vink notations.[44] However, the observed Co reduction suggests that the F doping process is accompanied by O desorption (Eq. 2).

$$O_O^{\times} + 2Co_{Co}^{\times} \rightarrow V_O^{\cdot\cdot} + \frac{1}{2}O_2(g) + 2Co_{Co}^{\prime} \quad (2)$$

Lattice O release is thermodynamically favorable under the conditions employed in this study, a low O_2 partial pressure atmosphere.[37] This process may be further promoted by the reducing nature of F sources such as PVDF, which can decompose and release reducing gases. The reductive F doping observed in this study is likely attributed to O desorption (Eq. 2) followed by F incorporation (Eq. 1). These reactions are possible because the pristine LSC64 thin film contains high-valence Co species. Assuming that the δ is 0, the formal valence number of Co is +3.4, allowing sufficient capacity for the reduction of Co ($Co^{4+} \rightarrow Co^{3+}$ and/or $Co^{3+} \rightarrow Co^{2+}$).

Since the O_2 activity was not controlled in this study, it is possible that differences in the reducing nature of the F sources altered the O vacancy concentration and electrical conductivity of the target sample. However, the clear correlation observed between the F source and the F concentration demonstrates that, while this correlation may include contributions from both the equilibrium a_{F_2} itself and O vacancy formation, F source selection is a critical parameter determining the F content. Furthermore, as evidenced by the non-uniform F distribution in the BiF_3-treated sample and the relatively uniform F distributions in the MgF_2- and PVDF-treated samples, appropriate selection of the F source is also essential from the perspective of controlling the homogeneity of F distribution.

3.2 Effects of reaction temperature

The reaction temperature is also a critical parameter determining the final F concentration and distribution homogeneity because it affects both the equilibrium a_{F_2} of the F sources and the diffusion rate of F^-. In this section, the effect of reaction temperature was systematically evaluated by heat treatment with MgF_2 at 240, 300, 350 or 500 °C for 10 h. As shown in Table 1, the equilibrium a_{F_2} of MgF_2 increases with temperature (240 °C: 7.94×10^{-106}, 300 °C: 7.03×10^{-94}, 350 °C: 1.10×10^{-85}, 500 °C: 1.75×10^{-67}). It should be noted that reaction temperature affects not only the equilibrium a_{F_2} of the F source but also the physical properties of the target material, such as electrical conductivity and O vacancy concentration. However, for experimental simplicity, the F source and target material were heat-treated simultaneously at the same temperature in this study.

SEM observations revealed that the surface morphology remained unchanged after the F doping for the samples treated at 240, 300, and 350 °C (Figs. 5a–5c). However, as shown in Fig. 5d, the 500 °C-treated sample exhibited surface precipitates, indicating side reactions at elevated temperature. Figure 5e shows the XRD patterns of samples treated at different temperatures. For samples treated at 240, 300, 350, and 500 °C, only peaks corresponding to the LSC64 perovskite phase and the YSZ substrate were observed, with no impurity phases from side reactions detected. The lattice parameters of samples treated at 240, 300, and 350 °C were 3.760, 3.788, and 3.779 Å, respectively (Table 1), all showing an increase compared to the pristine sample (3.729 Å). The degree of lattice expansion was maximum at 300 °C and slightly decreased at 350 °C. The lattice parameter of the 500 °C-treated sample was 3.749 Å, which decreased to nearly the same level as the pristine sample (3.729 Å). As shown in Fig. 5f, clear XPS F1s peaks were observed from the 240 °C-, 300 °C- and 350 °C-treated samples, indicating the high F concentrations at the surfaces. Notably, the 500 °C-treated sample exhibited a significantly reduced F1s intensity, indicating a substantial decrease in surface F concentration.

As shown in Fig. 6, TOF-SIMS depth profiles showed that the F^- intensity in the bulk region followed the order 240 °C < 350 °C < 300 °C, consistent with the lattice parameter trend. In contrast, for

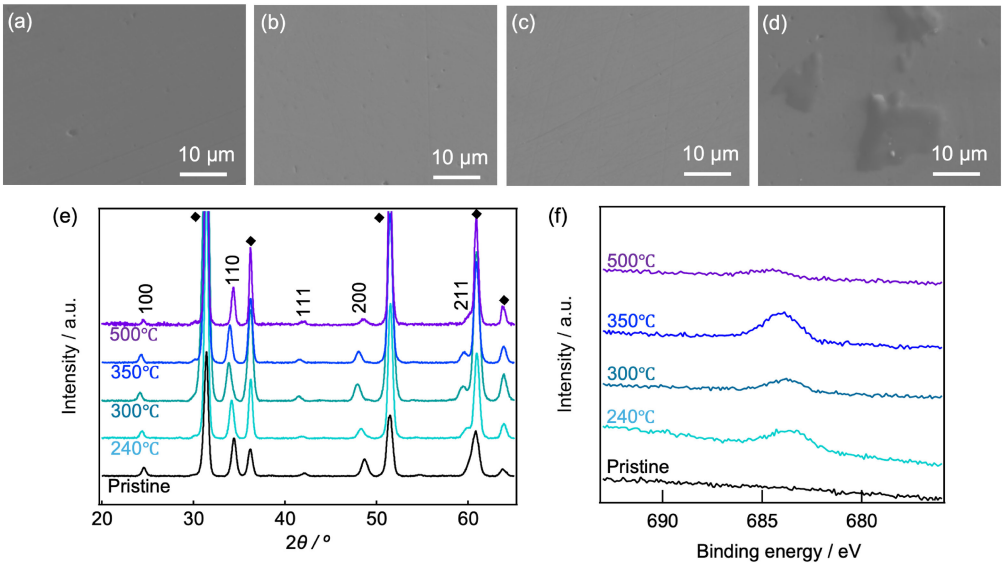

Figure 5. SEM images showing the top surface of the F-doped LSC64 thin films treated with MgF_2 at (a) 240 °C, (b) 300 °C, (c) 350 °C or (d) 500 °C for 10 h. (e) XRD patterns of the pristine and the F-doped LSC64 samples. The LSC64 peaks were indexed based on the cubic perovskite structure with space group $Pm\bar{3}m$. The symbol (◆) represents YSZ (substrate) peaks. (f) XPS F1s spectra of each sample.

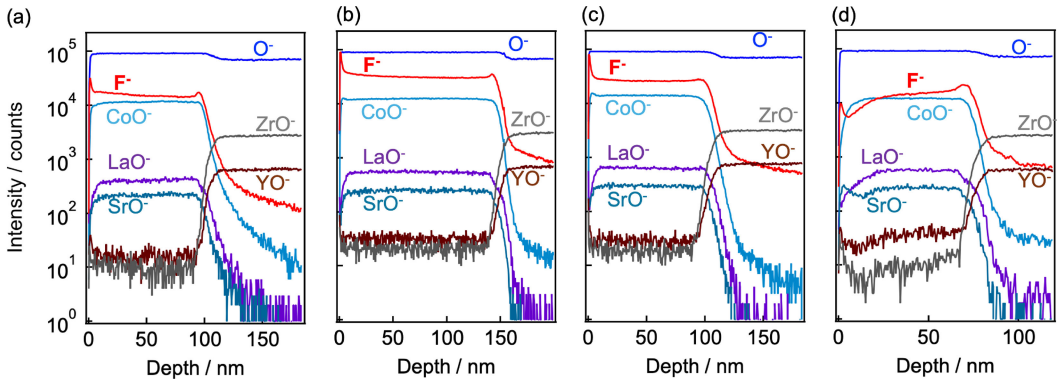

Figure 6. In-depth elemental profiles evaluated by TOF-SIMS of the F-doped LSC64 thin films treated with MgF_2 at (a) 240 °C, (b) 300 °C, (c) 350 °C or (d) 500 °C for 10 h.

the 500 °C sample, the bulk F^- intensity was lower than those of the other samples. The intensities of LaO^- and CoO^- near the surface decreased compared to other samples, while the intensities of SrO^- and F^- locally increased. This result suggests the formation of stable fluoride phases such as SrF_2 on the surface, indicating partial decomposition of the LSC64 perovskite structure. This is consistent with the side reactions suggested by SEM observations (Fig. 5d).

The bulk F concentration ratios ($C_F/(C_{La} + C_{Sr})$) measured by EPMA were 0.22, 0.29, 0.26, and 0.09 for the samples treated at 240, 300, 350, and 500 °C, respectively (Table 1). The F concentration was maximum at 300 °C and decreased in the order of 350 °C, 240 °C, and 500 °C. This trend does not necessarily correlate with the increase in equilibrium a_{F_2} (240 °C < 300 °C < 350 °C < 500 °C), indicating that F desorption or side reactions become dominant at temperatures above 300 °C. In our experimental setup, since the sample and the F source were set at the same temperature, higher temperatures generally increase the O vacancy concentration, which could enhance F incorporation.[37] However, the observed decrease in F concentration above 300 °C suggests that at high temperatures, the thermal instability of F has a greater influence than the O vacancy concentration on determining the final F concentration.

Figure 7 shows the Co *K*-edge XAS spectra. The degree of Co reduction in each sample followed the order 300 °C ≈ 350 °C < 240 °C < pristine, which corresponded to the F concentration. Furthermore, this suggests F incorporation accompanied by O desorption (Eq. 2) as discussed in the F-source experiment section.

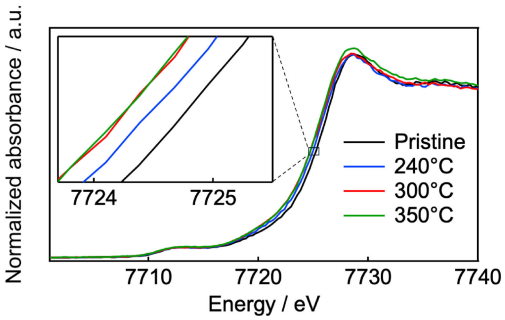

Figure 7. XANES spectra of Co *K*-edge of the pristine and the F-doped LSC64 thin films treated with MgF_2 at 240, 300, or 350 °C for 10 h. The inset shows the expanded spectra around the absorption edge.

TOF-SIMS depth profiles revealed that the homogeneity of F distribution also depends on temperature (Fig. 6). The 240 °C-treated sample showed a slight gradient in F^- intensity from the

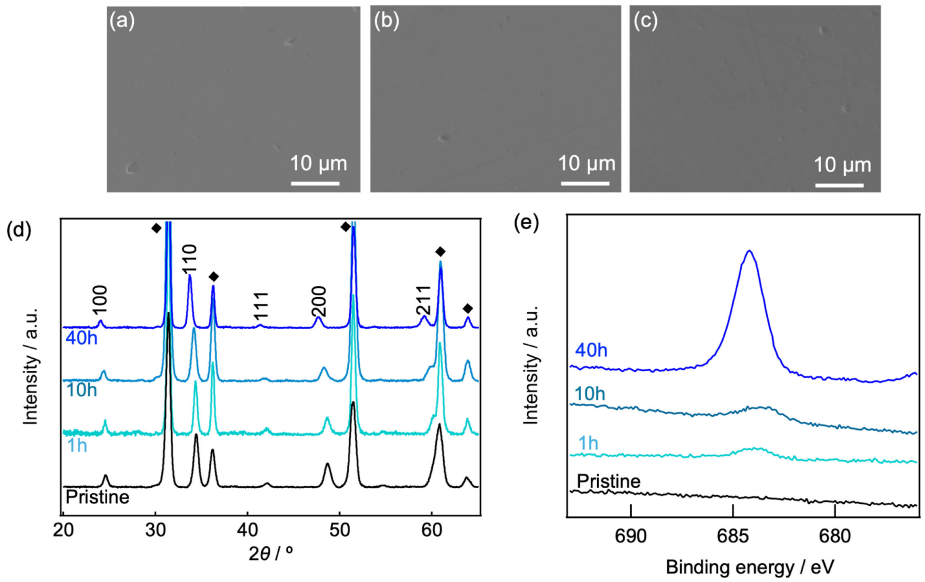

Figure 8. SEM images showing the top surface of the F-doped LSC64 thin films treated with MgF_2 at 240 °C for (a) 1 h, (b) 10 h or (c) 40 h. (d) XRD patterns of the pristine and the F-doped samples. The LSC64 peaks were indexed based on the cubic perovskite structure with space group $Pm\bar{3}m$. The symbol (◆) represents YSZ (substrate) peaks. (e) XPS F1s spectra of each sample.

surface to the bulk, whereas the 300 °C- and 350 °C-treated samples exhibited more uniform F distribution throughout the film thickness. This improvement is attributed to the increased diffusion coefficient of F^- with rising temperature. In contrast, the 500 °C-treated sample showed inhomogeneous distribution with localized F^- intensity enhancement near the surface probably due to any side reactions as mentioned above.

These results clearly demonstrate the existence of an optimal temperature range for topochemical F doping. At 300 °C, the increased equilibrium a_{F_2} and moderate diffusion rate achieve higher F concentration and uniform F distribution compared to 240 °C. At 350 °C, despite the even higher equilibrium a_{F_2}, F concentration slightly decreases compared to 300 °C due to F desorption or destabilization within the structure. At 500 °C, F desorption and the formation of stable phases such as SrF_2 might significantly reduce the F concentration in the perovskite structure.

Interestingly, the F concentration of the MgF_2-treated sample at 300 °C was nearly equivalent to that of the PVDF-treated sample at 240 °C shown in the previous section. This indicates that comparable F concentrations can be achieved by appropriate control of reaction temperature, even when using different F sources. However, since the O_2 activity was not controlled during the F doping process in this study, samples with the same F concentration may have different O concentrations depending on the reaction conditions.

These results demonstrate that selecting an appropriate temperature range (around 300 °C in this system) is crucial for obtaining F-doped materials with controlled F concentration and uniform distribution, by balancing the equilibrium a_{F_2} of the F source, the diffusion rate of F^-, and the thermal stability of F in the host structure.

3.3 Effects of reaction time

The reaction time is also a critical parameter determining the final F concentration and distribution homogeneity, because it affects both the amount of F supplied from the F source via gas-phase and the diffusion distance of F^- into the thin film interior. In this section, the effect of reaction time was evaluated by heat treatment with MgF_2 at 240 °C for 1, 10, and 40 h to elucidate the kinetic aspects of the F doping process.

SEM observations showed that all F-doped film surfaces were relatively smooth regardless of reaction time, indicating minimal impact of the F doping treatment on surface morphology (Figs. 8a–8c). Figure 8d shows the XRD patterns of these samples. For all samples, only peaks corresponding to the YSZ substrate and the LSC64 perovskite phase were observed, and no crystalline impurity phases were detected. The position of the LSC64 peaks systematically shifted toward lower angles with increasing reaction time. The lattice parameters obtained by refinement were 3.736, 3.760 and 3.804 Å for the 1, 10 and 40 h-treated samples, respectively (Table 1). The degree of lattice expansion increased monotonically with reaction time. The 40 h-treated sample showing the largest lattice expansion among all samples prepared in this study.

As shown in Fig. 8e, XPS F1s peaks were observed in all the samples, confirming that F incorporation into the surface proceeds even with only 1 h of treatment. The F1s peak intensity increased with reaction time and was maximum for the 40 h-treated sample. TOF-SIMS analysis (Fig. 9) showed that the bulk F^- intensity increased with reaction time. The bulk F-concentration ratios ($C_F/(C_{La} + C_{Sr})$) measured by EPMA were 0.05, 0.22, and 0.43 for the 1, 10 and 40 h-treated samples, respectively (Table 1). The F concentration increased monotonically with reaction time, showing no signs of saturation, unlike the temperature dependence observed in the previous section. As shown in the Co *K*-edge XANES spectra (Fig. 10), the degree of Co reduction increased with longer reaction time. The Co reduction was observed even in the 1 h-treated sample, which indicates that O desorption occurs from the early stages of the F doping reaction.

Furthermore, TOF-SIMS depth profiles revealed that relatively uniform F distribution was achieved throughout the entire film thickness (100–150 nm) even with only 1 hour of treatment. (Fig. 9). If the process was diffusion-limited, a typical diffusion profile with exponentially decreasing concentration from the surface to the bulk would be observed. However, the observed nearly uniform F distribution strongly suggests that the F doping process is limited by the F incorporation reaction at the surface or the F supply rate from the gas phase when MgF_2 was used as the F source. This behavior means that F diffusion in LSC64 is fast like O diffusion in LSC64.[38] This feature explains why topochemical F doping proceeds efficiently.

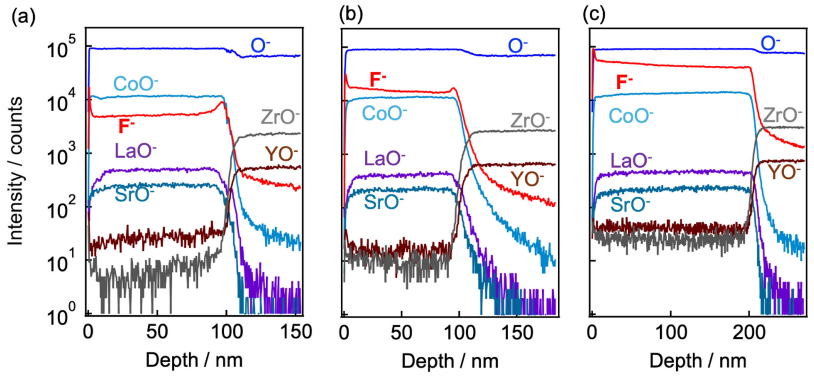

Figure 9. In-depth elemental profiles evaluated by TOF-SIMS of the F-doped LSC64 thin films treated with MgF_2 at 240 °C for (a) 1 h, (b) 10 h or (c) 40 h.

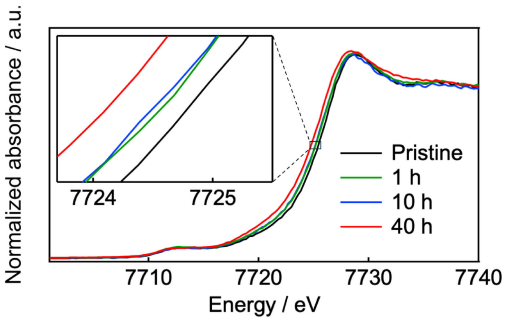

Figure 10. XANES spectra of Co *K*-edge of the pristine and the F-doped LSC64 thin films treated with MgF_2 at 240 °C for 1 h, 10 h or 40 h. The inset shows the expanded spectra around the absorption edge.

These results indicate that optimization of reaction time is important for controlling F concentration. Although F incorporation throughout the entire film thickness is possible even with short-time (1 h) treatment, long-time (40 h) treatment is required to obtain high F concentrations.

Interestingly, the F concentration ratio, $C_F/(C_{La} + C_{Sr})$, of the MgF_2-treated sample at 240 °C for 40 h was 0.43, which exceeded those of the PVDF-treated sample at 240 °C for 10 h (0.33, F source section) and the MgF_2-treated sample at 300 °C for 10 h (0.29, temperature section). This demonstrates that high F concentrations can be achieved by extending the reaction time, even with low equilibrium a_{F_2} (low temperature or weak F source). Conversely, using high equilibrium a_{F_2} (high temperature or strong F source) enables reaching the target F concentration in a shorter time.

Therefore, in designing practical F-doping conditions, comprehensive optimization of three parameters is necessary: F source, temperature, and reaction time. While LSC64 was used as a model case in this study, the identified correlations between reaction conditions and F-doping behavior are expected to be applicable to other mixed ionic-electronic conducting materials. The insights obtained in this study provide guidelines for rational selection of reaction conditions of topochemical anion doping to achieve precise control of anion composition and functional properties.

4. Conclusion

In this study, we experimentally investigated the effects of the F sources, reaction temperatures, and reaction times on the topochemical F doping to $La_{0.6}Sr_{0.4}CoO_{3-\delta}$ thin films to establish guidelines for precise control of anion composition in topochemical anion doping processes. The investigation revealed the following effects of each condition.

Regarding the F source, although changes in O vacancy concentration during the reaction may also contribute, our results demonstrate that the F source is a critical factor determining the F concentration in the product. The findings suggest that the F concentration is governed by the equilibrium a_{F_2} of the F source. However, as observed in the large F concentration gradient in the BiF_3-treated sample, the choice of F source can affect the homogeneity of F distribution. Regarding temperature, an optimal temperature range exists where maximum F concentration is obtained (300 °C in this study). Although higher temperatures generally increase the O vacancy concentration, which could enhance F incorporation, the observed decrease in F concentration above 300 °C indicates that the thermal instability of F in the LSC64 structure has a greater influence, leading to F desorption and decomposition reactions. Regarding time, it was found that F concentration increases with increasing time. Furthermore, when MgF_2 was used as the F source, it was found that the topochemical F doping process is governed by surface reaction kinetics rather than bulk diffusion limitations.

The knowledge obtained in this study provides practical guidelines for optimizing topochemical F doping conditions through comprehensive consideration of F sources, temperatures, and reaction times. While these insights were obtained by using LSC64 as a model material, they are expected to be applicable to diverse mixed ionic-electronic conducting materials, enabling precise compositional control in topochemical anion doping and contributing to the rational design of anion-doped functional materials with tailored properties.

Acknowledgment

This work was supported in part by JSPS KAKENHI (Grant No. 24KJ0371 and 24H02205).

CRediT Authorship Contribution Statement

Takuya Katsumata: Conceptualization (Lead), Data curation (Lead), Formal analysis (Lead), Funding acquisition (Lead), Investigation (Lead), Methodology (Lead), Writing – original draft (Lead), Writing – review & editing (Equal)
Chayathorn Lawthaweesawat: Conceptualization (Equal), Data curation (Lead), Formal analysis (Lead), Writing – review & editing (Equal)
Mahunnop Fakkao: Supervision (Supporting), Writing – review & editing (Equal)
Yuta Kimura: Supervision (Supporting), Writing – review & editing (Equal)
Takashi Nakamura: Funding acquisition (Equal), Supervision (Equal), Writing – review & editing (Equal)
Koji Amezawa: Funding acquisition (Supporting), Supervision (Equal), Writing – review & editing (Equal)

Conflict of Interest

The authors declare no conflict of interest in the manuscript.

Funding

Japan Society for the Promotion of Science: 24KJ0371
Japan Society for the Promotion of Science: 24H02205

References

1. H. Kageyama, K. Hayashi, K. Maeda, J. P. Attfield, Z. Hiroi, J. M. Rondinelli, and K. R. Poeppelmeier, *Nat. Commun.*, **9**, 772 (2018).
2. K. Maeda, F. Takeiri, G. Kobayashi, S. Matsuishi, H. Ogino, S. Ida, T. Mori, Y. Uchimoto, S. Tanabe, T. Hasegawa, N. Imanaka, and H. Kageyama, *Bull. Chem. Soc. Jpn.*, **95**, 26 (2022).
3. U. Breddemann and I. Krossing, *ChemElectroChem*, **7**, 1389 (2020).
4. C. Yang, Y. Tian, C. Yang, G. Kim, J. Pu, and B. Chi, *Adv. Sci.*, **10**, 2304224 (2023).
5. M. Li, H. Liu, and L. Feng, *Electrochem. Commun.*, **122**, 106901 (2021).
6. J. Lu, B. Cao, B. Hu, Y. Liao, R. Qi, J. Liu, C. Zuo, S. Xu, Z. Li, C. Chen, M. Zhang, and F. Pan, *Small*, **18**, 2103499 (2022).
7. J. Kim, J. Lee, S. Kim, and W. Jung, *Electron. Mater. Lett.*, **20**, 450 (2024).
8. T. Katsumata, S. Kobata, Y. Watase, R. Aso, S. Yagi, Y. Kimura, K. Amezawa, and T. Nakamura, *ACS Appl. Nano Mater.*, **8**, 21215 (2025).
9. J. Ran, T. Wang, J. Zhang, Y. Liu, C. Xu, S. Xi, and D. Gao, *Chem. Mater.*, **32**, 3439 (2020).
10. T. Uyama, K. Mukai, and I. Yamada, *Electrochemistry*, **89**, 94 (2021).
11. C. Tassel, Y. Goto, D. Watabe, Y. Tang, H. Lu, Y. Kuno, F. Takeiri, T. Yamamoto, C. M. Brown, J. Hester, Y. Kobayashi, and H. Kageyama, *Angew. Chem., Int. Ed. Engl.*, **55**, 9667 (2016).
12. K. Shao, D. Zhou, M. Yang, H. Zhu, H. Fan, and T. Su, *J. Alloys Compd.*, **977**, 173413 (2024).
13. J. Zhu, X. Zuo, and Z. Fang, *J. Nanosci. Nanotechnol.*, **20**, 6422 (2020).
14. C. K. Blakely, S. R. Bruno, S. K. Kraemer, A. M. Abakumov, and V. V. Poltavets, *J. Solid State Chem.*, **289**, 121490 (2020).
15. S. Feng, X. Rao, X. Chen, F. Ning, M. Wang, and Y. Liu, *Process Saf. Environ. Prot.*, **191**, 2026 (2024).
16. A. Kanno, Y. Ugata, I. Ikeuchi, M. Hibino, K. Nakura, Y. Miyaoka, I. Kawamura, D. Shibata, T. Ohta, and N. Yabuuchi, *ACS Energy Lett.*, **8**, 2753 (2023).
17. X. Xu, L. Pi, J.-J. Marie, G. J. Rees, C. Gong, S. Pu, R. A. House, A. W. Robertson, and P. G. Bruce, *J. Electrochem. Soc.*, **168**, 080521 (2021).
18. T. Uchimura, F. Takeiri, K. Okamoto, T. Saito, T. Kamiyama, and G. Kobayashi, *J. Mater. Chem. A*, **9**, 20371 (2021).
19. T. Katsumata, H. Yamamoto, Y. Kimura, K. Amezawa, R. Aso, S. Kikkawa, S. Yamazoe, and T. Nakamura, *Adv. Funct. Mater.*, **33**, 2307116 (2023).
20. R. Aso, T. Katsumata, T. Nakamura, Y. Watase, K. Amezawa, and Y. Murakami, *Microscopy*, **73**, 22 (2024).
21. R. Sun, H. Li, D. Zhang, Z. Liu, Y. Ma, D. Meng, and C. Zhao, *Chem. Commun.*, **60**, 15043 (2024).
22. M. A. Hayward, E. J. Cussen, J. B. Claridge, M. Bieringer, M. J. Rosseinsky, C. J. Kiely, S. J. Blundell, I. M. Marshall, and F. L. Pratt, *Science*, **295**, 1882 (2002).
23. K. Wissel, J. Heldt, P. B. Groszewicz, S. Dasgupta, H. Breitzke, M. Donzelli, A. I. Waidha, A. D. Fortes, J. Rohrer, P. R. Slater, G. Buntkowsky, and O. Clemens, *Inorg. Chem.*, **57**, 6549 (2018).
24. T. Katayama, A. Chikamatsu, Y. Hirose, R. Takagi, H. Kamisaka, T. Fukumura, and T. Hasegawa, *J. Mater. Chem. C*, **2**, 5350 (2014).
25. Y. Kobayashi, O. J. Hernandez, T. Sakaguchi, T. Yajima, T. Roisnel, Y. Tsujimoto, M. Morita, Y. Noda, Y. Mogami, A. Kitada, M. Ohkura, S. Hosokawa, Z. Li, K. Hayashi, Y. Kusano, J. eun Kim, N. Tsuji, A. Fujiwara, Y. Matsushita, K. Yoshimura, K. Takegoshi, M. Inoue, M. Takano, and H. Kageyama, *Nat. Mater.*, **11**, 507 (2012).
26. R. Mikita, T. Aharen, T. Yamamoto, F. Takeiri, T. Ya, W. Yoshimune, K. Fujita, S. Yoshida, K. Tanaka, D. Batuk, A. M. Abakumov, C. M. Brown, Y. Kobayashi, and H. Kageyama, *J. Am. Chem. Soc.*, **138**, 3211 (2016).
27. T. Yajima, F. Takeiri, K. Aidzu, H. Akamatsu, K. Fujita, W. Yoshimune, M. Ohkura, S. Lei, V. Gopalan, K. Tanaka, C. M. Brown, M. A. Green, T. Yamamoto, Y. Kobayashi, and H. Kageyama, *Nat. Chem.*, **7**, 1017 (2015).
28. R. Porhiel, B. Clavier, T. Karakoç, S. Pronkin, D. Foix, E. Petit, M. El-Ghozzi, and K. Guérin, *Batteries*, **11**, 53 (2025).
29. U. Breddemann, J. Sicklinger, F. Schipper, V. Davis, A. Fischer, K. Huber, E. M. Erickson, M. Daub, A. Hoffmann, C. Erk, B. Markovsky, D. Aurbach, H. A. Gasteiger, and I. Krossing, *Batter. Supercaps*, **4**, 632 (2021).
30. J. Jacobs, M. A. L. Marques, H. C. Wang, E. Dieterich, and S. G. Ebbinghaus, *Inorg. Chem.*, **60**, 13646 (2021).
31. J. O. Binder, S. P. Culver, R. Pinedo, D. A. Weber, M. S. Friedrich, K. I. Gries, K. Volz, W. G. Zeier, and J. Janek, *ACS Appl. Mater. Interfaces*, **10**, 44452 (2018).
32. B. Gonano, Ø. S. Fjellvåg, G. Steciuk, K. Marshall, H. Fjellvåg, and M. Valldor, *Scr. Mater.*, **255**, 116379 (2025).
33. H. Yamamoto, K. Tada, J. Hwang, D. Hirai, Z. Hiroi, K. Matsumoto, and R. Hagiwara, *Inorg. Chem.*, **62**, 2116 (2023).
34. Y. Tsujimoto, K. Yamaura, N. Hayashi, K. Kodama, N. Igawa, Y. Matsushita, Y. Katsuya, Y. Shirako, M. Akaogi, and E. Takayama-Muromachi, *Chem. Mater.*, **23**, 3652 (2011).
35. C. K. Blakely, J. D. Davis, S. R. Bruno, S. K. Kraemer, M. Zhu, X. Ke, W. Bi, E. E. Alp, and V. V. Poltavets, *J. Fluorine Chem.*, **159**, 8 (2014).
36. Y. Ma, Y. Zhu, Y. Yang, Q. Liu, S. Hu, S. Hu, and L. Chen, *Dalton Trans.*, **54**, 8298 (2025).
37. M. Kuhn, S. Hashimoto, K. Sato, K. Yashiro, and J. Mizusaki, *J. Solid State Chem.*, **197**, 38 (2013).
38. M. V. Ananyev, N. M. Porotnikova, and E. K. Kurumchin, *Solid State Ionics*, **341**, 115052 (2019).
39. H. Miura, *J. Crystallogr. Soc. Jpn.*, **45**, 145 (2003).
40. Thermodynamic database MALT group, *Thermodynamic Database MALT for Windows, 2005 (CD-ROM)*, Kagaku Gijutsu-Sha, https://www.kagaku.com/malt/
41. F. Tanaka, L. Gungaajav, O. Terakado, S. Kuzuhara, and R. Kasuya, *Thermochim. Acta*, **702**, 178977 (2021).
42. J. E. Marshall, A. Zhenova, S. Roberts, T. Petchey, P. Zhu, C. E. J. Dancer, C. R. McElroy, E. Kendrick, and V. Goodship, *Polymers*, **13**, 1354 (2021).
43. Y. Orikasa, T. Ina, T. Nakao, A. Mineshige, K. Amezawa, M. Oishi, H. Arai, Z. Ogumi, and Y. Uchimoto, *J. Phys. Chem. C*, **115**, 16433 (2011).
44. F. A. Kröger and H. J. Vink, *Solid State Phys.*, **3**, 307 (1956).